Supplementary Information (SI) for Sustainable Energy & Fuels.
This journal is © The Royal Society of Chemistry 2026

Supporting information:

Push-pull electronic effects of three-component two-heterojunction electrocatalyst for directional carrier transport in bifunctional water electrolysis

Ankit Sharma,[a] Nitul Kalita, and Mohammad Qureshi[a]*

[a]*Department of Chemistry, Indian Institute of Technology Guwahati, 781039, Assam, India*

*email: mq@iitg.ac.in

1. Supporting materials characterizations:

1.1. Energy Dispersive Spectroscopy (EDS) analysis:

The elemental composition and spatial distribution of the synthesized catalyst were evaluated using Energy Dispersive X-ray Spectroscopy (EDS). The elemental composition is derived from characteristic X-ray emissions produced when high-energy electrons interact with the sample, with each element generating a distinctive X-ray signature at a specific energy level. Elemental mapping confirms the uniform spatial distribution of the constituent elements, including Nickel (Ni), Cobalt (Co), Oxygen (O), Sulfur (S), and Phosphorus (P), across the designated scanning electron microscopy (SEM) area. Furthermore, the quantitative analysis derived from the EDS spectrum provides the specific weight percentages (Weight%) of these detected elements, confirming the successful incorporation of all precursor components into the hierarchical heterostructure.

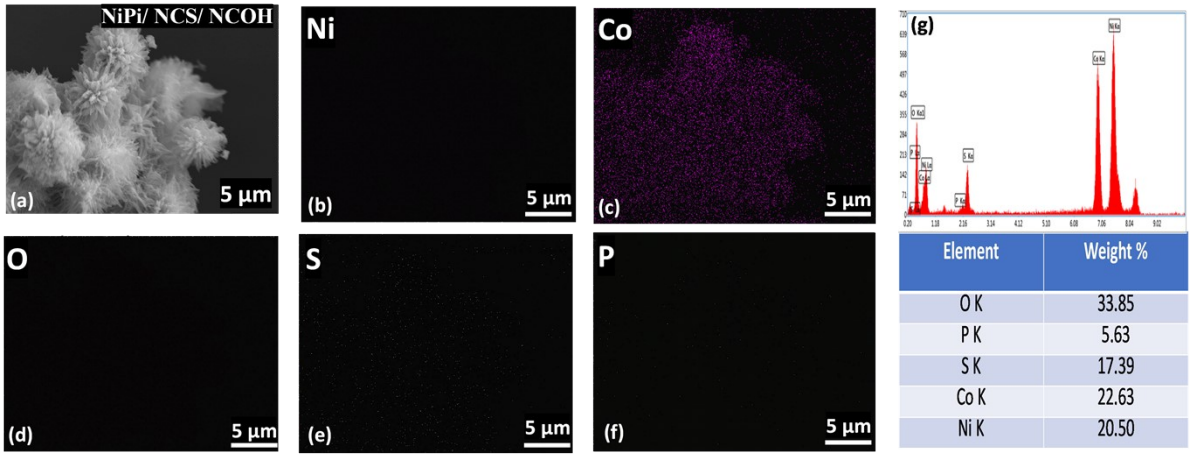

Element	Weight %
O K	33.85
P K	5.63
S K	17.39
Co K	22.63
Ni K	20.50

Figure S1: Energy Dispersive X-ray Spectroscopy (EDS) elemental mapping images corresponding to the SEM area (a), demonstrating the spatial distribution of (b) Nickel (Ni), (c) Cobalt (Co), (d) Oxygen (O), (e) Sulfur (S), and (f) Phosphorus (P). (g) The corresponding EDS spectrum and a quantitative table listing the weight percentages (Weight%) of the detected elements.

1.2. X-ray Photoelectron Spectroscopy (XPS) analysis:

The X-ray photoelectron spectroscopy (XPS) analysis provides detailed information about the elemental composition, oxidation states, and surface electronic structure of the catalytic materials. The survey spectra (Figure S2a) for NCOH, NCS/NCOH, and the NiPi/NCS/NCOH heterostructure confirm the presence of Ni, Co, O, S, and P in their respective compounds. Key elemental regions, including P 2p, S 2p, O 1s, Co 2p, and Ni 2p, highlight the specific electronic environments within the multi-component system. Figure S2 (b) presented high-resolution XPS spectra O 1s for all electrodes with three distinct peaks at 530 eV, 531.1eV and 531.9 eV corresponding to $O_{lattice}$ (metal-oxygen bonds), O_{vac} (oxygen vacancies) and O_{ads} (surface-adsorbed oxygen).

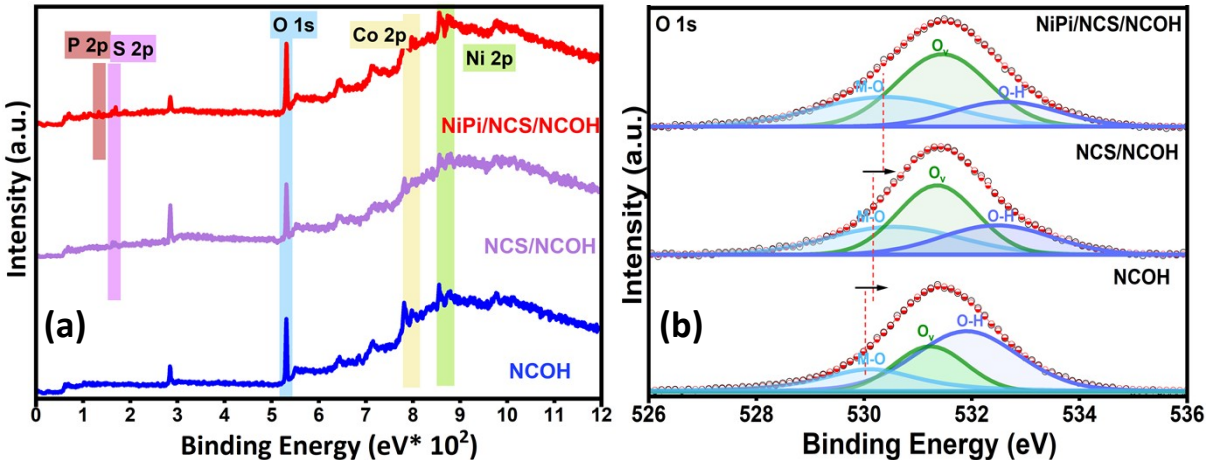

Figure S2: X-ray Photoelectron Spectroscopy (XPS) analysis of the electrocatalysts. (a) XPS survey spectra comparing the elemental composition of NCOH (blue), NCS/NCOH (purple), and the NiPi/NCS/NCOH (red) heterostructure. The spectra confirm the presence of all constituent elements, including Nickel (Ni 2p), Cobalt (Co 2p), Oxygen (O 1s), Sulfur (S 2p), and Phosphorus (P 2p), with specific core-level regions highlighted to demonstrate the successful formation of the three-component system. (b) Deconvoluted high-resolution O 1s XPS spectra for NCOH, NCS/NCOH, and NiPi/NCS/NCOH.

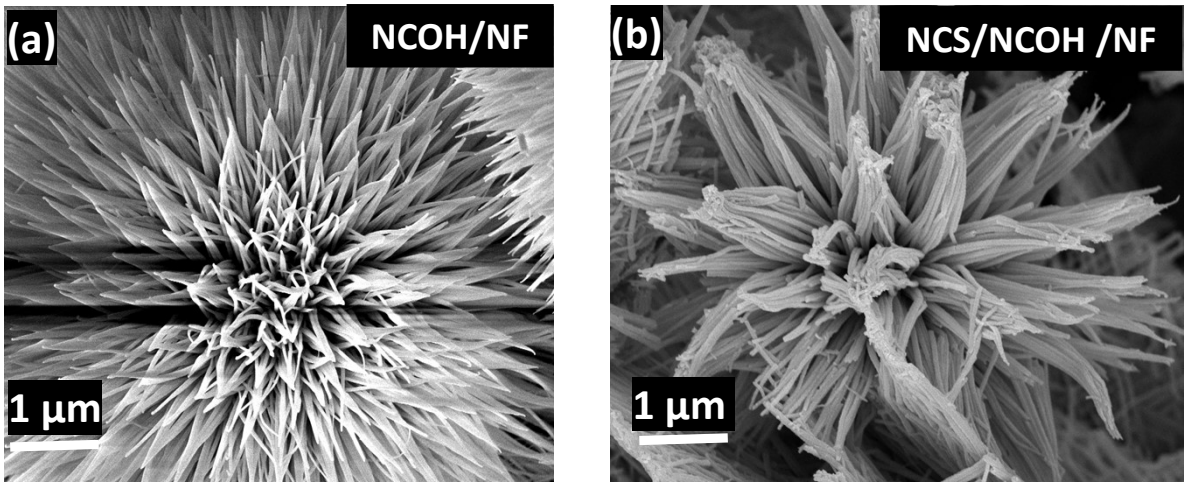

1.3 Field Emission Scanning Electron Microscopy (FESEM) analysis

Figure S3: FESEM images (a) NCOH/NF, (b)NCS/NCOH/NF

According to the FESEM image of NCOH (Figure S3a), a uniform and dense layer of vertically aligned nanosheets is formed over nickel foam. These nanosheets assemble into complex, sea urchin-like morphology, a morphology that is typical for metal hydroxide. In the second step, the NCOH undergoes a solvothermal sulfidation by treatment with Na_2S at 150°C. The resulting NCS/NCOH (Figure S3b) retains its hierarchical, nanosheet-based structure, but the nanosheets display a more textured morphology.

1.4. Fourier Transform Infrared Spectroscopy (FT-IR) analysis

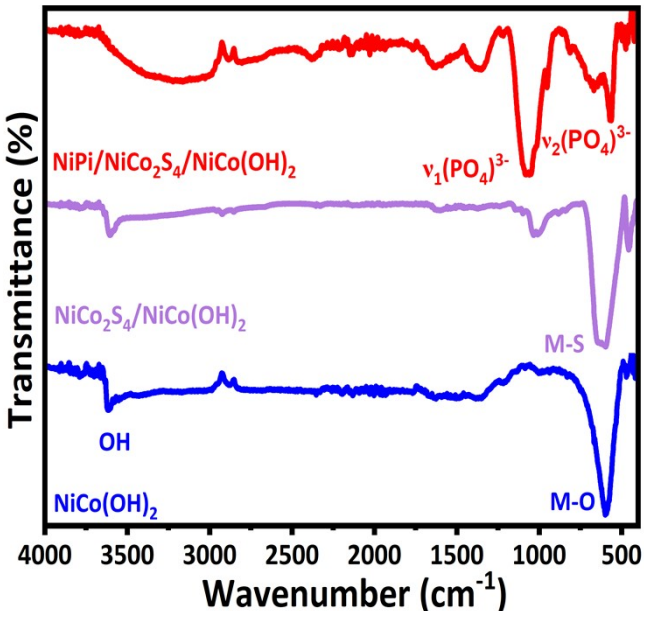

Figure S4: FTIR spectra of NCOH, NCS/NCOH and NiPi/NCS/NCOH

In FTIR spectra (Figure S4), NCOH shows a broad absorption at 3400 $cm^{-1,}$ which represents O-H stretching from hydroxyl groups and adsorbed water, while a sharp signal at 500-600 cm^{-1} corresponds to M-O and M-OH vibrational modes characteristic of the bimetallic hydroxide lattice. In the NCS/NCOH composite, these bands persist alongside emerging metal–sulfur (M-S) stretches in the low-wavenumber region. The ternary NiPi/NCS/NCOH catalyst exhibits a distinctive strong peak between 1000 and 1100 cm^{-1}, assigned to asymmetric stretching (v_1) of phosphate ions (PO_4^{3-}), while peak at 530 cm^{-1} corresponds to O-P-O bending vibration, validating the formation of the triple-component heterostructure

1.5 BET isotherm and BJH pore size distribution

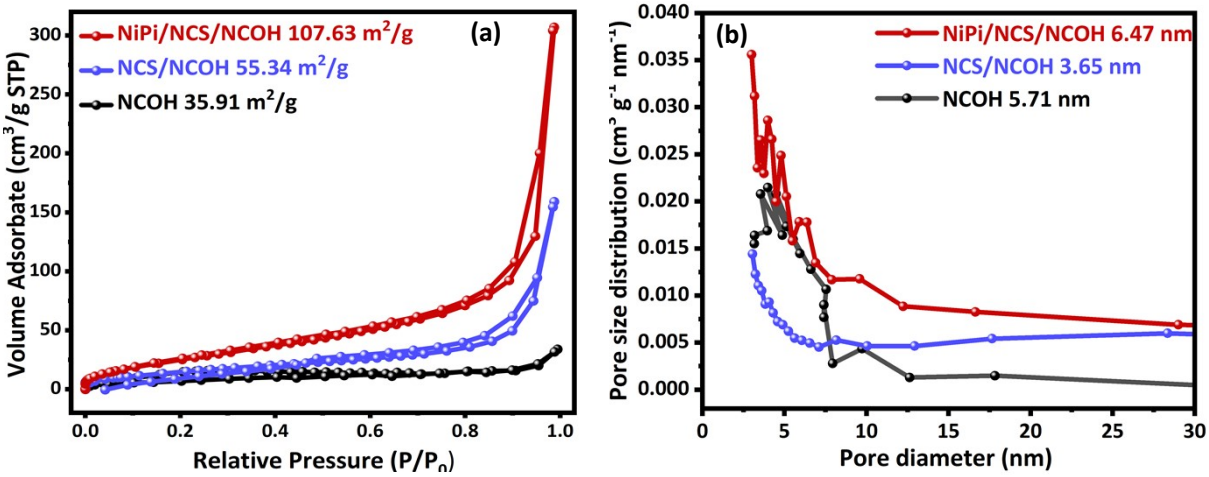

Figure S5: Nitrogen (N_2) adsorption-desorption analysis of NiPi/NCS/NCOH, NCS/NCOH, and NCOH: (a) N_2 adsorption–desorption isotherms; (b) BJH pore size distribution curves.

Catalyst	BET surface area (S_{BET} m^2/g)	Avg pore size (nm)
NiPi/NCS/NCOH	107.63	6.47
NCS/NCOH	55.34	3.65
NCOH	35.91	5.71

To investigate the specific surface area and porous nature of the synthesized electrocatalysts, adsorption-desorption measurements were conducted. As shown in Figure S5(a), all samples exhibit Type IV isotherms with a distinct hysteresis loop in the high relative pressure region

($P/P_0 > 0.4$), which is characteristic of a mesoporous structure. The Brunauer-Emmett-Teller (BET) specific surface area of the ternary NiPi/NCS/NCOH heterostructure was calculated to be 107.63 $m^2 g^{-1}$, which is significantly higher than those of the binary NCS/NCOH (55.34 $m^2 g^{-1}$) and pristine NCOH (35.91$m^2 g^{-1}$). This substantial enhancement in surface area is attributed to the hierarchical coupling of the amorphous NiPi with the crystalline NCS/NCOH framework, effectively preventing the aggregation of the components and providing a greater density of exposed active sites.

Furthermore, the Barrett-Joyner-Halenda (BJH) pore size distribution curves in Figure S5(b) reveal that the majority of pores are distributed within the mesoporous range, with average pore diameters of 6.47 nm, 3.65 nm, and 5.71 nm for NiPi/NCS/NCOH, NCS/NCOH, and NCOH, respectively. The combination of a high specific surface area and an optimized mesoporous channel network in the NiPi/NCS/NCOH composite is expected to facilitate rapid mass transport of electrolyte ions and efficient gas release, thereby playing a crucial role in enhancing its overall electrocatalytic performance for water splitting.

1.6 Electronic Band Structure and UPS Analysis

To investigate the electronic band alignment and energy level positions of the synthesized materials, Ultraviolet Photoelectron Spectroscopy (UPS) was employed. Figures S6(a), (b), and (c) present the UPS spectra for $NiCo(OH)_2$, $NiCo_2S_4$ and $Ni_3(PO_4)_2$(NiPi), respectively. The valence band maximum (E_{VB}) for each sample was determined by linear extrapolation of the leading edge of the valence band region to the baseline. The E_{VB} values relative to the Fermi level (E_F= 0 eV) were found to be 1.45 eV for $NiCo(OH)_2$, 1.58 eV fo $NiCo_2S_4$, and 2.7 eV for $Ni_3(PO_4)_2$(NiPi). By incorporating the optical band gap (E_g) values derived from UV-Vis diffuse reflectance spectra, the conduction band minimum (E_{CB}) positions were calculated using the relation $E_{CB}= E_{VB} - E_g$. As illustrated in the schematic energy band diagram in Figure S6 (d), the positions are located at -1.5 eV, -0.43 eV, and -0.7 eV for $NiCo(OH)_2$, $NiCo_2S_4$ and $Ni_3(PO_4)_2$, respectively. This comparative energy level analysis reveals a staggered band alignment between the components, which is critical for facilitating efficient charge carrier separation and migration across the heterostructure interfaces during electrocatalytic processes.

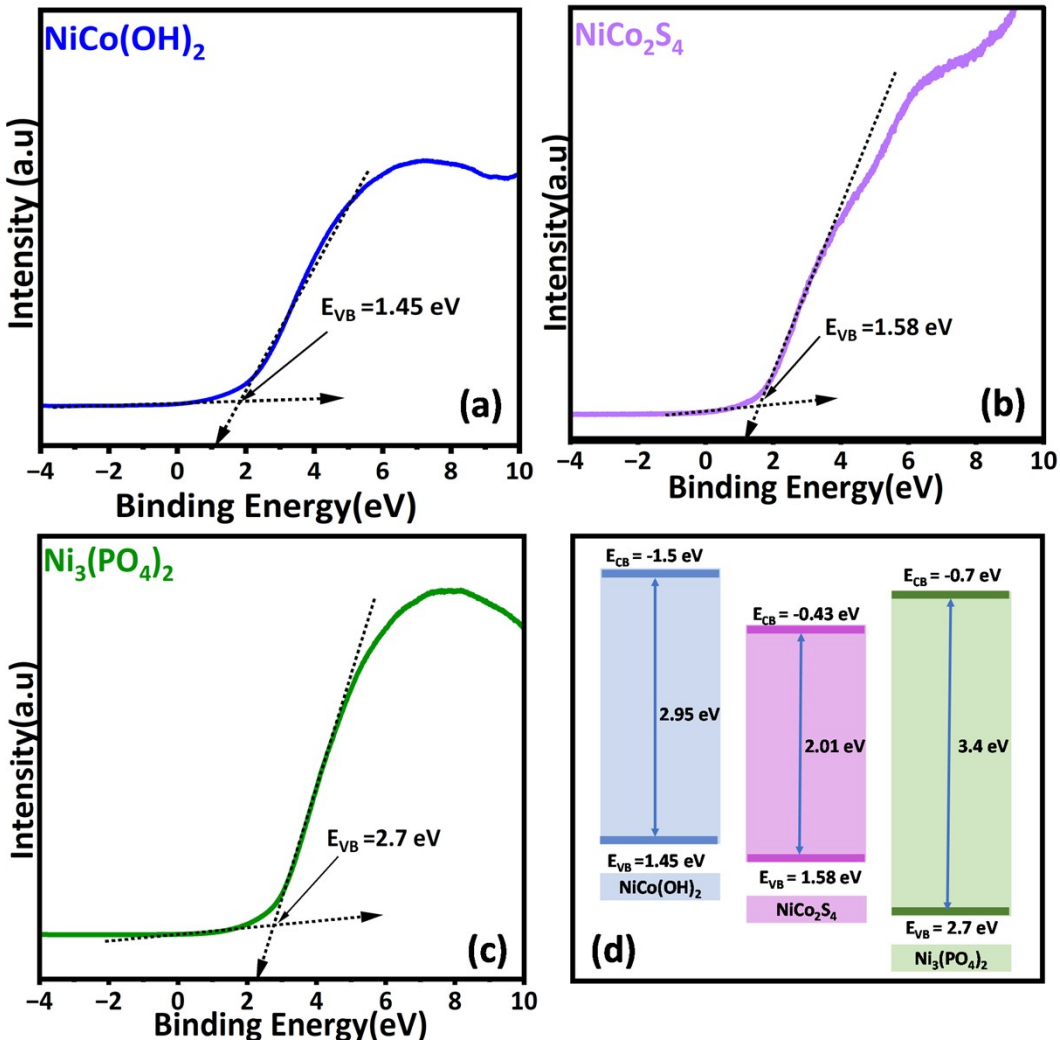

Figure S6: Ultraviolet photoelectron spectroscopy (UPS) spectra of $NiCo(OH)_2$, $NiCo_2S_4$ and $Ni_3(PO_4)_2$, equilibrium energy band alignment diagram for the NiPi/NCS/NCOH heterojunction, based on E_{VB} from UPS data and Band gap from tauc plots.

2. Electrochemical measurements

2.1. Overpotential calculations:

Linear sweep voltammetry (LSV) was conducted over a voltage range of 1.6 V to 0 V for OER and -1.4 V to 0 V for HER versus the Hg/HgO reference electrode at a scan rate of 5 mV s^{-1}. The overpotential (η) values for all the catalysts were determined at a standard current density of 10 mA cm^{-2} using the following equation S1&2):

$$\eta_{10}(OER) = (E_{obs} - 1.23)V\ versus\ RHE \quad \text{... (S1)}$$

$$\eta_{10}(HER) = (E_{obs} - 0)V\ versus\ RHE \quad \text{... (S2)}$$

Electrochemical Impedance Spectroscopy (EIS) measurements were conducted, with the resulting Nyquist plots presented in Figure S7a. The plots for all electrodes display a characteristic semicircle in the high-frequency region, where the diameter of the semicircle corresponds directly to the charge transfer resistance (R_{ct}) at the electrode-electrolyte interface. Notably, the NiPi/NCS/NCOH heterostructure exhibits a smaller semicircle diameter compared to NCOH, NiPi, and the NCS/NCOH. This reduction in R_{ct} indicates that the construction of the hierarchical heterostructure effectively enhances the intrinsic electrical conductivity and facilitates faster electron transport.

To investigate the impact of varying electrodeposition CV cycles of NiPi on the electrochemical performance, a set of electrocatalytic evaluations for both OER and HER was performed as shown in Fig. S7b and S7c. Among the different cycle numbers examined (10, 15, 20, and 25 cycles), the sample synthesized with 20 cycles exhibited best catalytic activity, reflected by its low overpotential and higher current density. This superior performance suggests that 20 cycles achieve an ideal balance of active material loading, promoting efficient charge transfer without introducing excessive resistance.

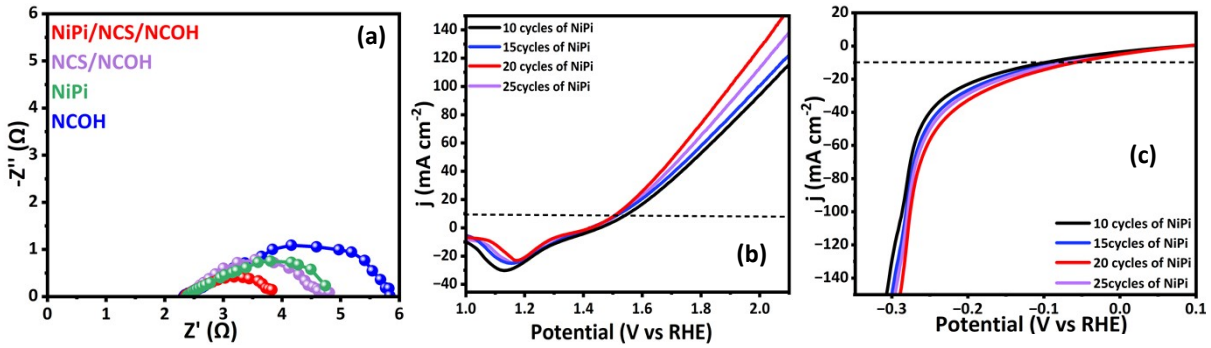

Figure S7: (a) Electrochemical Impedance Spectroscopy (EIS) Nyquist plots comparing the charge transfer resistance (Rct) of NCOH, NiPi, NCS/NCOH, and the NiPi/NCS/NCOH heterostructure. (b) Linear Sweep Voltammetry (LSV) curves for the Oxygen Evolution Reaction (OER) and (c) Hydrogen Evolution Reaction (HER) of NiPi/NCS/NCOH. Both panels compare the catalytic effect of NiPi deposition, samples prepared with varying electrodeposition cycles of NiPi in NiPi/NCS/NCOH (10, 15, 20, and 25 cycles).

2.2. Tafel slope calculations:

The Tafel slope was determined by using the relationship between overpotential and the logarithm of current density (log j) using equation S3:

$$\eta = b\log\left(\frac{j}{j_o}\right) \quad \text{... (S3)}$$

where "*b*" is the Tafel slope, "*j*" implies the current density, and "j_o" is the exchange current density.

2.3. Distribution of Relaxation Times (DRT):

DRT Methodologies: The Distribution of Relaxation Times (DRT) analysis was conducted using DRT Tools, an open-source MATLAB-based software. The DRT plots were generated utilising a Gaussian basis function with a regularization parameter of 0.01.

The Distribution of Relaxation Times (DRT) method effectively analyses electrochemical impedance spectroscopy (EIS) data by examining how charge carriers return to equilibrium under varying applied frequencies, improving the precision of interpretations across different time scales. The corresponding time constant (τ) is determined using the expression $\tau = 1/2\pi f$, where f denotes the frequency. This time constant is an intrinsic characteristic of each process and remains independent of the surface area. The relaxation times observed, along with the associated charge transfer processes in the systems, arises mainly from four fundamental electrochemical phenomena: Ohmic contact (R_o), charge transfer resistance (R_{ct}), and concentration gradients that influence diffusion properties within the electrode materials or electrolyte. By deconvoluting the EIS spectra using DRT, multiple peaks were identified in the γ(Ω) versus τ(s) plot, representing distinct kinetic processes that occur during the reaction. The area under each peak represents the magnitude of the polarization resistance of a specific process.

2.4. Determination of the electrochemically active surface area (ECSA):

Electrochemically active surface area (ECSA) data extracted from cyclic voltammetry measurements in the non-Faradaic region demonstrate the comparative availability of active sites across the three catalyst systems. The double-layer capacitance (C_{dl}), which provides a direct estimation of the ECSA, was obtained by plotting the difference in current density ($\Delta J_0 = j_{anodic} - j_{cathodic}$) of the fabricated electrodes (NiPi, NCS/NCOH and NiPi/NCS/NCOH) as a function

of the scan rate. Cyclic voltammetry (CV) was conducted in a non-faradaic region (0.59 V to 0.69 V vs. R.H.E) versus Hg/HgO reference electrode, with scan rates varying from 2 to 10 mV s^{-1} (figure S8a-c). The center of working potential (i.e., 0.64 V) was selected to calculate ΔJ_0 (vs. Hg/HgO). The formula used for the determination of ECSA is as shown in equation S4.

$$ECSA = \frac{C_{dl}}{C_s} \quad \text{... (S4)}$$

Here, C_{dl} represents the double-layer capacitance, while C_s denotes the specific capacitance of the material. Typically, an average C_s value of 0.040 mF cm^{-2} is used.

The NiPi, NCOH, and NiPi/NCS/NCOH composite materials display distinct C_{dl} values (Figure S8d), with the composite (NiPi/NCS/NCOH) heterostructure exhibiting the highest capacitance, indicating superior site accessibility and increased catalytic surface area. The linear relationship between the current difference and scan rate confirms the purely capacitive behavior in this potential window, validating the ECSA calculations. Higher ECSA values in the composite material correlate with improved catalytic performance, as more active sites are available for water oxidation/reduction reactions.

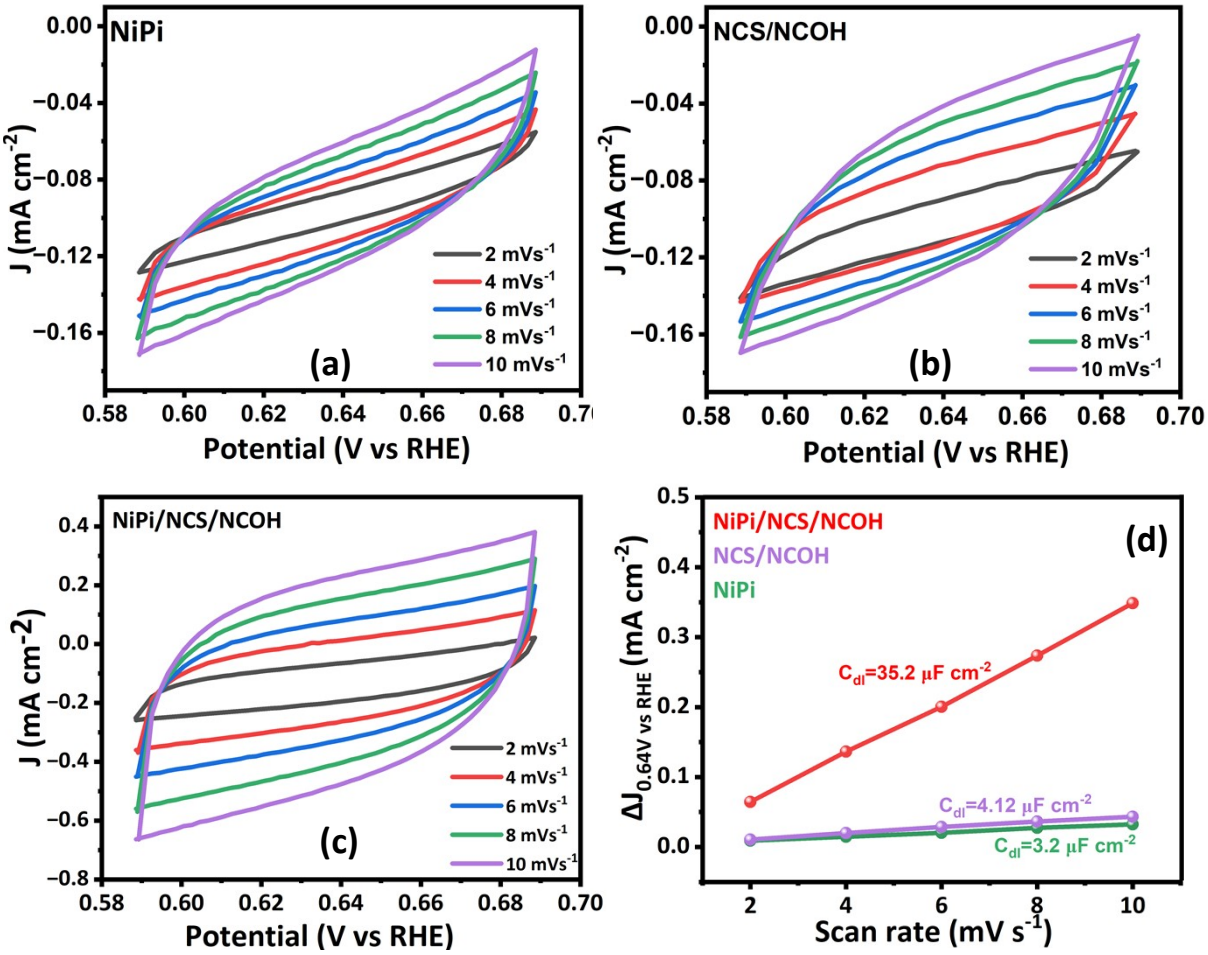

Figure S8: CV plots for (a) NiPi, (b) NCS/NCOH, and (c) the NiPi/NCS/NCOH composite material. non-faradaic potential window ranging from 0.59 V to 0.69 V vs. RHE at various scan rates 2, 4, 6, 8, and 10 mV s^{-1}:(d) Current density vs. scan rate plots for determining the C_{dl} values of NiPi, NCS/NCOH and NiPi/ NCS/NCOH

2.5. Determination Turnover Frequency (TOF) from OER Current Density:

TOF values were calculated assuming that the surface-active metal ions that had undergone the redox reaction just before the onset of OER only participated in OER electrocatalysis. The corresponding expression is

$$TOF = (j \times N_A)/(F \times n \times \Gamma) \quad \text{...(S5)}$$

Where, j= current density, N_A= Avogadro number, F = Faraday constant, n = Number of electrons transferred during the reaction, Γ= Surface concentration of the catalyst.

TOF calculation for NCOH

Calculated area associated with the reduction of Ni^{3+} to Ni^{2+} of NCOH

= 0.000016 V A

Hence, the associated charge is = 0.000016 V A /0.01 V s^{-1}

= 0.0016 A s

= **0.0016 C**

Now, the number of electrons transferred is

= 0.0016 C / 1.602 * 10^{-19} C

= **0.1* 10^{17}**

Since, the reduction of Ni^{3+} to Ni^{2+} is a single electron transfer reaction, the number electron calculated above is exactly the same as the number of surface-active sites.

Hence, the number of Ni participants in OER = **0.1* 10^{17}**

For determining Turnover frequency was calculated assuming that the Ni atoms that had undergone the redox reaction just before the onset of OER only and participated in OER electrocatalysis. Therefore, from the equation S5:

$$TOF = \left[\left(1.6 \times 10^{-3}\right)\left(6.022 \times 10^{23}\right)\right]/[(96485)(4)(0.1 \times 10^{17})$$

=0.24 s^{-1}

TOF calculation for NCS/NCOH

Calculated area associated with the reduction of Ni^{3+} to Ni^{2+} of NCS/NCOH

=0.00002545 V A

Hence, the associated charge is = 0.0000254 V A /0.01 V s^{-1}

= 0.00254 A s

= **0.00254 C**

Now, the number of electrons transferred is

= 0.00254 C /1.602 * 10^{-19} C

= **0.159* 10^{17}**

Since the reduction of Ni^{3+} to Ni^{2+} is a single electron transfer reaction, the number electron calculated above is the same as the number of surface-active sites.

Hence, the number of Ni participating in OER = **0.159* 10^{17}**

For determining Turnover frequency was calculated assuming that the Ni atoms that had undergone the redox reaction just before the onset of OER only and participated in OER electrocatalysis. Therefore, from the equation S5

$$TOF = \left[(5.2 \times 10^{-3})(6.022 \times 10^{23})\right]/[(96485)(4)(0.159 \times 10^{17})$$

=0.50 s^{-1}

TOF calculation for NiPi

Calculated area associated with the reduction of Ni^{3+} to Ni^{2+} of NiPi

=0.000037 V A

Hence, the associated charge is = 0.00037 V A /0.01 V s^{-1}

= 0.0037 A s

= **0.0037 C**

Now, the number of electrons transferred is

= 0.0037 C /1.602 * 10^{-19} C

= **0.237* 10^{17}**

Since the reduction of Ni^{3+} to Ni^{2+} is a single electron transfer reaction, the number electron calculated above is the same as the number of surface-active sites.

Hence, the number of Ni participating in OER = **0.237* 10^{17}**

For determining Turnover frequency was calculated assuming that the Ni atoms that had undergone the redox reaction just before the onset of OER only and participated in OER electrocatalysis. Therefore, from the equation S5

$$TOF = \left[(12 \times 10^{-3})(6.022 \times 10^{23})\right]/[(96485)(4)(0.237 \times 10^{17})$$

=0.79 s^{-1}

TOF calculation for NiPi/NCS/NCOH

Calculated area associated with the reduction of Ni^{3+} to Ni^{2+} of NiPi/NCS/NCOH

=0.00007 V A

Hence, the associated charge is = 0.00007 V A /0.01V s^{-1}

= 0.007 A s

= **0.007 C**

Now, the number of electrons transferred is

= 0.007 C /1.602 * 10^{-19} C

= **0.436 * 10^{17}**

Since the reduction of Ni^{3+} to Ni^{2+} is a single electron transfer reaction, the number electron calculated above is the same as the number of surface-active sites.

Hence, the number of Ni participating in OER = **0.436 * 10^{17}**

For determining Turnover frequency was calculated assuming that the Ni atoms that had undergone the redox reaction just before the onset of OER only and participated in OER electrocatalysis. Therefore, from the equation S5

$$TOF = \left[\left(25 \times 10^{-3}\right)\left(6.022 \times 10^{23}\right)\right]/[(96485)(4)(0.436 \times 10^{17})$$

=0.9 s^{-1}

2.6. Evaluation of Intrinsic Electrocatalytic Activity

To further evaluate the intrinsic electrocatalytic activity of the prepared electrodes independently of their physical surface area, Linear Sweep Voltammetry (LSV) curves were normalized by the Electrochemically Active Surface Area (ECSA), as shown in Figure S9. The ECSA-normalized current density (j_{ECSA}) provides a direct comparison of the catalytic efficiency per active site for NiPi/NCS/NCOH, NCS/NCOH, and pristine NCOH. As illustrated, the ternary heterostructure exhibits a significantly higher and more cathodic onset potential compared to both the binary and the single-component.

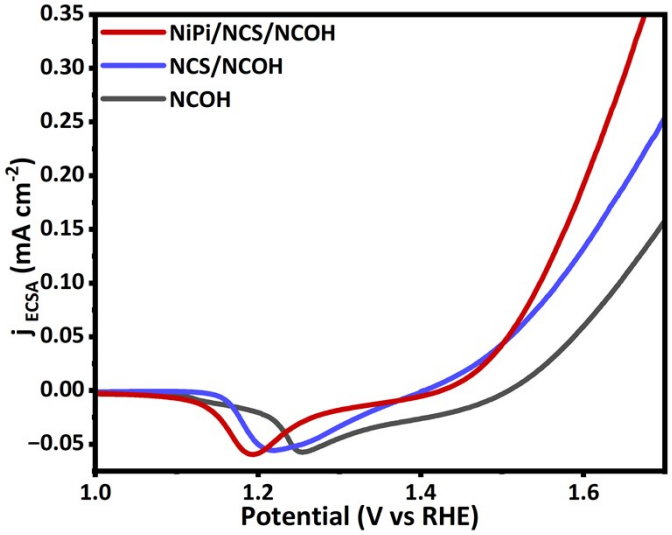

Figure S9: ECSA-normalised OER linear sweep voltammograms (j_{ECSA} vs. potential) for NiPi/NCS/NCOH (red), NCS/NCOH (blue), and NCOH (grey) in 1 M KOH, normalised by the electrochemically active surface area derived from double-layer capacitance (C_{dl}) measurements.

2.7. Mott-Schottky analysis:

Mott–Schottky analysis was performed in the neutral medium to verify the semiconductor behaviour of NCOH, NCS, and NiPi. The flat-band potential (E_{FB}) was calculated from the following equation S6:

$$\frac{1}{C^2} = \left(\frac{2}{e\varepsilon_0\,\varepsilon_r N_D A^2}\right)\left(V - V_{FB} - \frac{kT}{e}\right) \quad \text{... (S6)}$$

where e is the electron charge, ε_r is the dielectric constant, ε_o is the permittivity of vacuum, N_D is the number of charge carrier density, V is the applied potential, V_{FB} is the flat band potential, k is the Boltzmann constant, T is room temperature, and A is the surface area of the film in contact with the electrolyte.

The NCOH sample (Figure S10a) exhibits a negative slope in the high-potential region, which is characteristic of a p-type semiconductor. The extrapolation of this linear fit to the potential axis yields flat band potential (V_{FB}) vs NHE. Both the NCS (Figure S10b) and NiPi (Figure S10c) samples display a positive slope across the measured potential range, confirming their nature as n-type semiconductors. These distinct semiconductor types (p-type NCOH and n-type NCS/NiPi) and their highly divergent values are crucial, as the resulting band alignment at the

hetero-interfaces dictates the formation of an internal electric field that drives efficient charge separation and transport in the final composite. The precise band edge positions were established through Mott-Schottky analysis in 1 M Na_2SO_4 aqueous solution using Ag/AgCl as the reference electrode and converted to NHE. Mott-Schottky analysis provides crucial insights into the semiconductor junction properties and electronic structure of NiPi/NCS/NCOH, n-n-p heterojunction. The distinctive inverted V-shaped curve in the composite material (Figure S10d) confirms the formation of a heterojunction combining n and p-type components

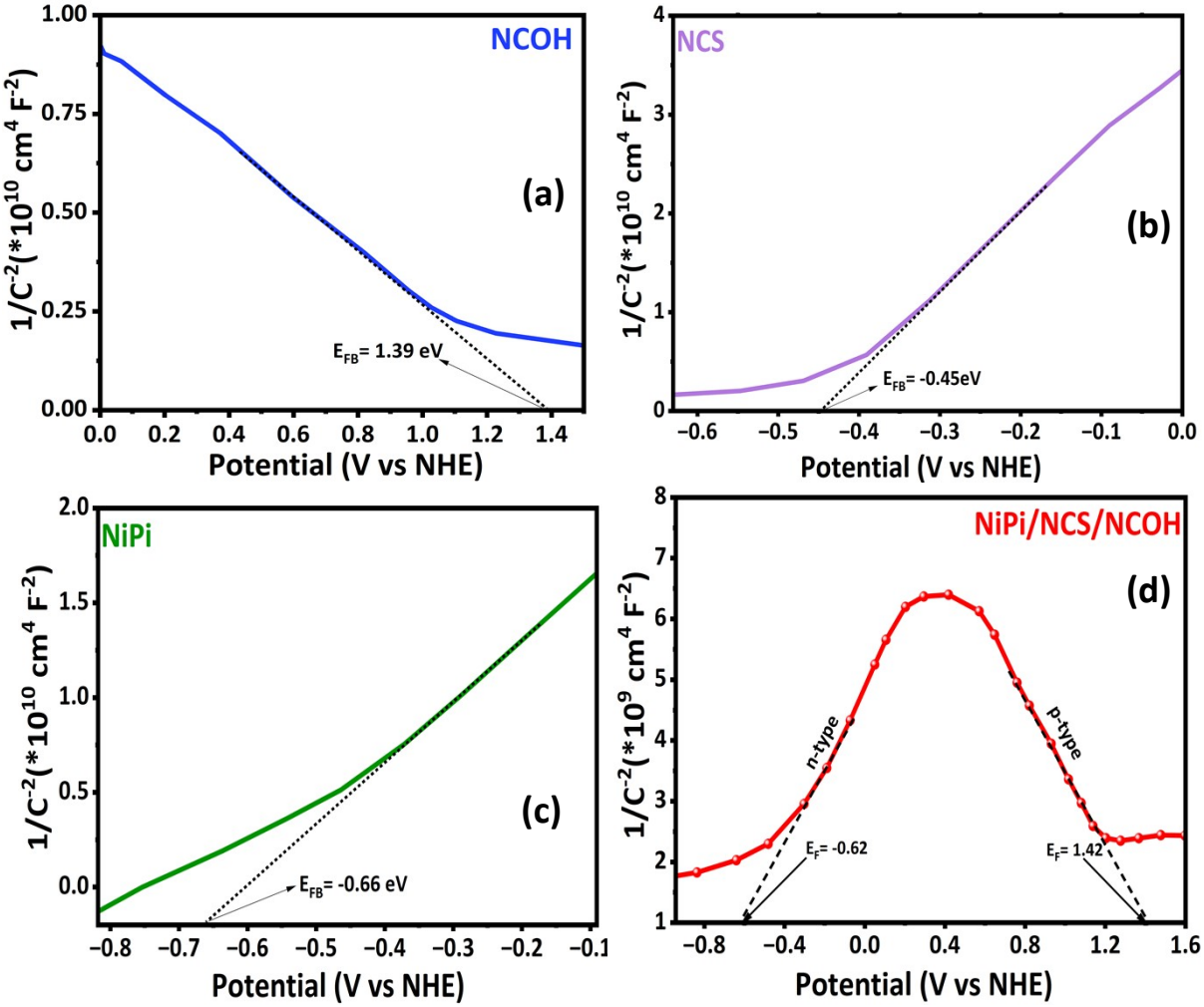

Figure S10: Mott-Schottky plot (a) NCOH, (b) NCS and (c) NiPi and (d) NiPi/NCS/NCOH with their flat band potential VS NHE.

2.8. Determination of charge carrier density (N_A):

$$\text{slope} = \left(\frac{-2}{e\varepsilon_0\,\varepsilon_r N_A A^2}\right) \quad \ldots (S7)$$

The value for ε_r was chosen as ~11 for NCOH, A = 1 cm^2, ε_0 = 8.8541 × 10^{-12} Fm^{-1}, and *e* = 1.602 × 10^{-19}C.

Slope is the slope of the Mott-Schottky plot (determined to be -6.64 × 10^8 & -5.81 ×10^8 for NCOH before and after the heterojunction formation, respectively. Therefore, from equation S7:

NCOH @Before Heterojunction formation

$$N_A = \frac{-2}{(1.6 * 10^{-19}) * (8.85 * 10^{-12}) * 11 * (-6.64 * 10^8)} = 1.93 * 10^{20} cm^{-3}$$

NCOH @After Heterojunction formation

$$N_A = \frac{-2}{(1.6 * 10^{-19}) * (8.85 * 10^{-12}) * 11 * (-5.81 * 10^8)} = 2.21 * 10^{20} cm^{-3}$$

This validates the charge transfer mechanism, evidenced by a significant increase in the carrier density (N_A) of NCOH from 1.93 ×10^{20} cm^{-3} to 2.21×10^{20} cm^{-3} following heterojunction formation as shown in Fig. S11. This accumulation confirms the transfer of holes from NCS to NCOH, thereby activating NCOH as a robust OER site.

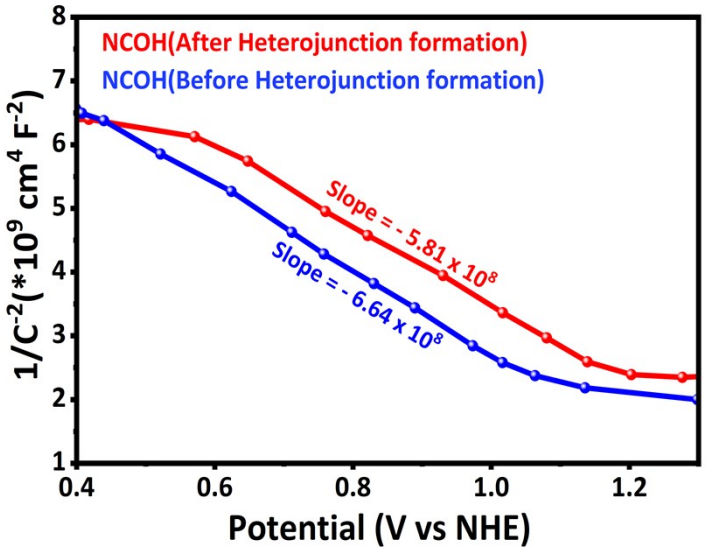

Figure S11: Mott-Schottky plot of NCOH before and after the heterojunction formation.

2.9. Chronoamperometry stability test

Long-term stability is a critical parameter for any practical electrocatalyst to assess its value in commercial applications. NiPi/NCS/NCOH catalyst was evaluated using chronoamperometry (Figure S12), at a constant current density of 10 mA/cm^2 for 60 hours. There was no significant degradation in performance,

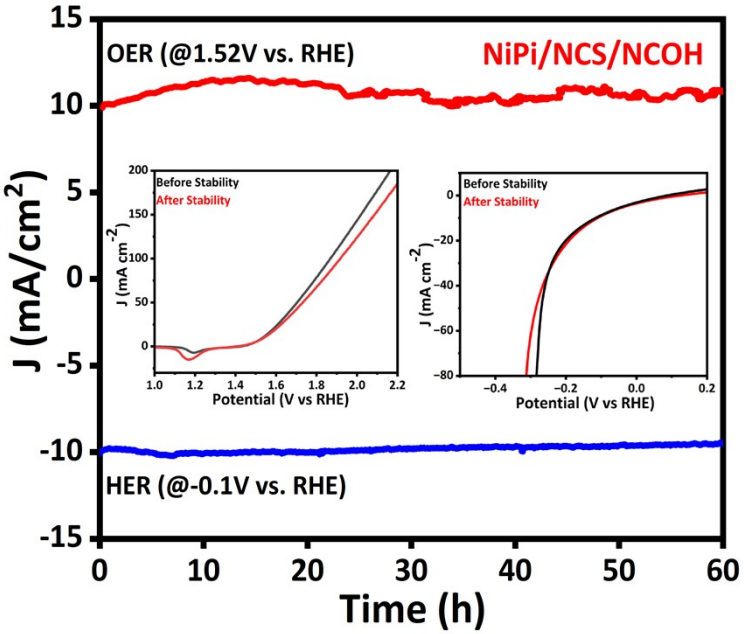

Figure S12: Chronoamperometry stability test at 10 mA cm^{-2} for 60 hours.

3. Determination of Faradaic yield:

Faradaic yield is defined as the ratio of the experimentally measured amounts of gases (H_2 and O_2) to their theoretically calculated quantities (equation S8).

$$Faradaic\ yield = \frac{Amount\ of\ gases\ evolved\ experimentally}{Amount\ of\ gases\ evolved\ theoretically} \quad \text{... (S8)}$$

The theoretical estimation of the gas evolved was performed using the following equation S9:

$$Amount\ of\ gases\ evolved\ theoretically = \frac{j \times t}{n \times F} \quad \text{...(S9)}$$

where *j* denotes the current density, *t* represents the time, *n* is the number of moles of charge required to produce one mole of gas (n = 2 for H_2 and n = 4 for O_2), and *F* is the Faraday constant (96485 C mol^{-1}). The experimentally evolved volume of evolved hydrogen and oxygen gases was monitored over 30 minutes using the inverted burette water displacement method. The average Faradaic yield for OER/HER was calculated to be 97% (±1%), indicating that the charge carriers generated in the system were completely utilised for the oxidation of H_2O molecules to produce O_2/H_2 gas.

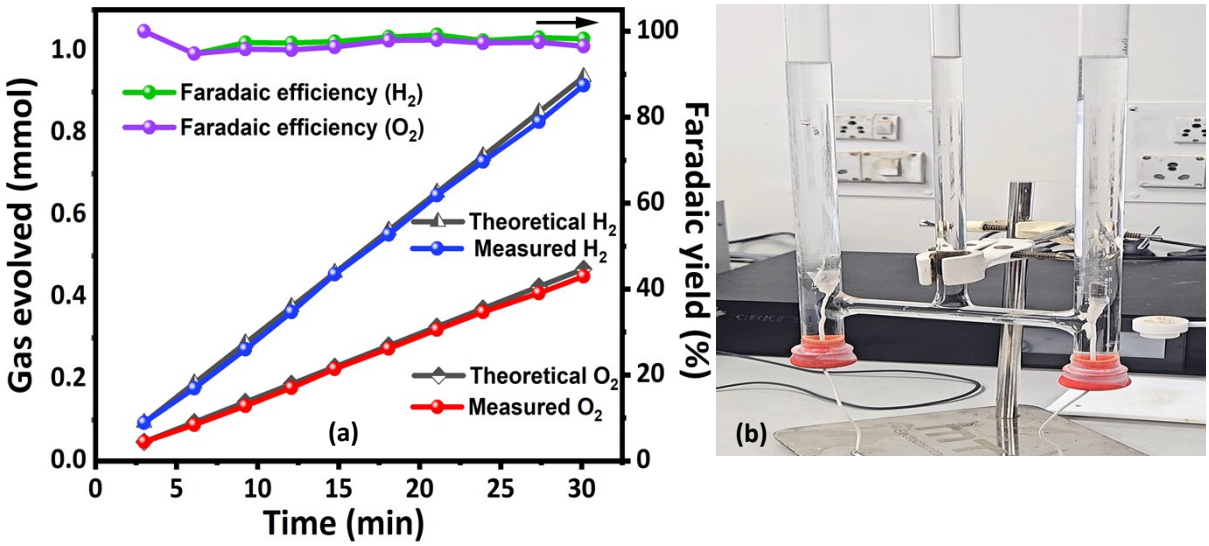

Figure S13: (a) Faradaic efficiency for hydrogen and oxygen at a current density of 10 mA cm^{-2}, for 30 minutes;(b) inverted burette water displacement setup.

4. Band gap calculations from Tauc plots:

Tauc plots serve as a tool for estimating the band gap energy (E_g) of materials by using the data of absorbance spectrum. It can be constructed using absorbance data acquired from

ultraviolet-visible diffuse reflectance spectroscopy (UV-Vis DRS) collected over a defined wavelength range (200-800 nm).

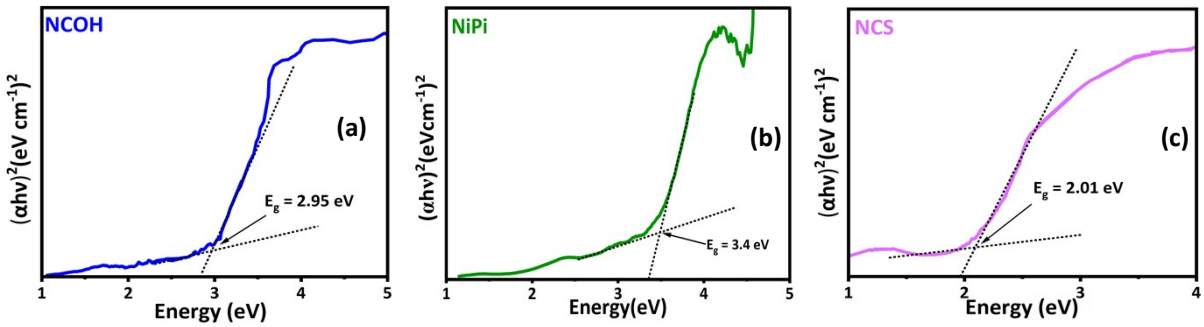

Figure S14: Tauc plots derived from UV-Vis diffuse reflectance spectra, used to determine the optical band gap energies (E_g) of the individual components: (a) NCOH, (b) NiPi, and (c) NCS, showing their respective band gaps.

5. Characterization after stability test:

Figure S15 (a) shows the X-ray diffraction pattern of NiPi/NCS/NCOH composite material before and after the 60 hours of stability test. The consistent X-ray diffraction pattern of the catalyst indicates that the catalyst retains its phase purity, demonstrating its robust structural integrity over prolonged operation. Figure S15b and S15c present the FESEM image of the NiPi/NCS/NCOH catalyst before and after the long-term stability test, which highlights that the morphology remains largely intact, signifying that the material is highly durable.

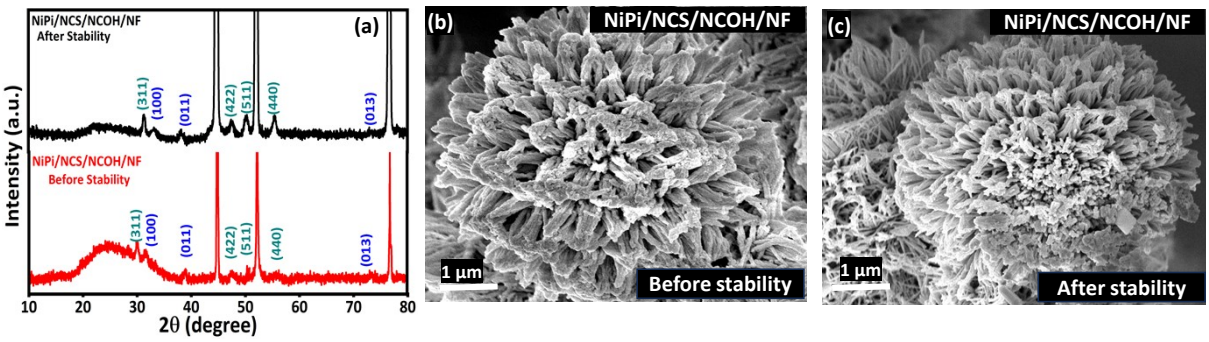

Figure S15: (a) XRD pattern of NiPi/NCS/NCOH before and after 60 hrs stability test; FESEM image of NiPi/NCS/NCOH (b) before stability test, (c) after stability test.

6.Electrocatalyst comparison table

Electrocatalysts	**Substrate**	**Electrolyte conc (KOH)**	**HER η_{10}**	**OER η_{10}**	**Tafel slope OER (mV dec^{-1})**	**Tafel slope HER (mV dec^{-1})**	**Ref**
NiPi/NCS/NCOH	**Ni foam**	**1 M**	**95**	**290**	**65**	**70**	**This work**
NiFe LDH/NiS_2/VS_2	Carbon cloth	1 M	76	286	99	79	1
Co-Fe phosphate	Not given	1 M	325	300	58.4	53.6	2
ZnFe LDH@NiCoS	Ni Foam	1M	246.3	284.8	85.7	74.6	3
$NiCo_2S_4$@Co_1Ni_4-LDH	Carbon cloth	1 M	200	306	46.3	56.8	4
S-NiCo-LDH	Carbon	1 M	168	235	83	89	5

	cloth						

References

1. T. Wang, X. Zhang, X. Yu, J. Li, K. Wang and J. Niu, Molecules, 2024, **29**, 951.
2. R. A. Qureshi, A. Ali, M. Y. Solangi, M. A. Shar, A. Alhazaa,I. A. Soomro, M. A. Qureshi, M. Kumar, H. M. Ansari, A.Hanan and U. Aftab, Int. J. Hydrogen Energy, 2025, **155**,150288.
3. M. Vedanarayanan, C. M. Chen and M. G. Sethuraman, ACSAppl. Energy Mater., 2024, 7(, **7**,260.
4. F. F. Yuan, J. D. Wei, G. X. Qin and Y. H. Ni, J. Alloys Compd.,2020, **830**, 154658.
5. Y. Cong, Q. Zheng, Y. Wang, J. Gao, S. Sun, X. Li and S.-W. Lv, ACS Appl. Mater. Interfaces, 2024, **16**, 64816.